Advanced Functional Materials

ADVANCED FUNCTIONAL MATERIALS
www.afm-journal.de

RESEARCH ARTICLE OPEN ACCESS

The Role of Ultra-Thin Buffer Layers for Achieving Ultra-Low Dark Currents in Single-Component Organic Photodetectors

Anncharlott Kusber[1] | Ying Sun[2] | Jakob Wolansky[1,3] | Louis Conrad Winkler[1,3] | Anna-Lena Hofmann[1] | Fred Kretschmer[1] | Hrisheekesh Thachoth Chandran[1] | Tianyi Zhang[1] | Mike Hambsch[4] | Stefan C. B. Mannsfeld[4] | Karl Leo[1] | Ji-Seon Kim[2,5,6] | Johannes Benduhn[1,3]

[1]Dresden Integrated Center For Applied Physics and Photonic Materials (IAPP) and Institute of Applied Physics, Technische Universität Dresden, Dresden, Germany | [2]Blackett Laboratory, South Kensington Campus, Imperial College London, South Kensington, London, UK | [3]Centre for Technology Development, German Centre for Astrophysics, Görlitz, Germany | [4]Center For Advancing Electronics Dresden and Faculty of Electrical and Computer Engineering, TUD Dresden University of Technology, Dresden, Germany | [5]Department of Chemistry, University of Oxford, Oxford, UK | [6]Department of Physics, Ewha Womans University, Seoul, Republic of Korea

Correspondence: Anncharlott Kusber (Anncharlott.kusber@tu-dresden.de) | Ji-Seon Kim (ji-seon.kim@imperial.ac.uk) | Johannes Benduhn (Johannes.benduhn@tu-dresden.de)

Received: 19 January 2026 | **Revised:** 27 April 2026 | **Accepted:** 27 April 2026

Keywords: buffer layer | dark current | detectivity | interface | organic photodetector | single-component

ABSTRACT

Single-component organic photodetectors (SC-OPDs), in which the active layer consists only of one organic material, show higher reproducibility and improved morphological stability. Their simplified architecture also provides a powerful platform for better isolating and understanding interfacial effects. Here, SubNc-based SC-OPDs incorporating an ultrathin (3 nm) PhOSubPc interfacial layer to control and probe the interaction between the SubNc absorber and the BPhen electron-transport layer (ETL) is investigated. The PhOSubPc layer acts as an energetic spacer, effectively decoupling SubNc energetically and morphologically from BPhen while maintaining high device performance. Ambient photoelectron spectroscopy (APS) confirms the energetic isolation of SubNc from BPhen, enabling a clear assessment of interfacial effects in single-component architectures. The optimized device achieves an EQE of 56% at 0 V, an ultra-low dark current density of $7.4 \cdot 10^{-12}$ A cm^{-2} at −0.1 V, and a specific detectivity D^* of $1.69 \cdot 10^{12}$ Jones at 0 V (based on measured noise). Due to their simplified single-component architecture, these SC-OPDs offer fundamental insight into interface effects, which result in state-of-the-art SC-OPD performance.

1 | Introduction

Photodetectors (PDs) convert light into an electrical signal and are foundational components in imaging, sensing, and optical communication [1, 2]. Silicon and indium gallium arsenide photodetectors have historically set the benchmark for optoelectronic performance and remain the current industry standard to this day, due to their high external quantum efficiency (EQE) and excellent noise characteristics, which, when combined, enable highly sensitive detection across the ultraviolet (UV) to near-infrared (NIR) spectrum [3–5]. Meanwhile, organic PDs (OPDs) have attracted considerable attention as feasible alternatives, offering advantages such as mechanical flexibility, tunable optoelectronic properties, low-cost processing, lightweight materials,

Anncharlott Kusber and Ying Sun contributed equally to this work.

and low-embodied energy manufacturing, while delivering competitive PD performance [6–10]. With advances in novel materials, device & interface engineering, and morphology control, OPDs can achieve specific detectivities (D^*) exceeding 10^{13} Jones, making them closely comparable to their inorganic counterparts [9, 11–13]. Nevertheless, under reverse bias, OPD performance is often limited by shot noise—one of the dominant contributions to the noise current i_{noise}, which scales directly with the square root of the dark current density ($\sqrt{J_D}$) and inversely with D^* [14].

Conventionally studied bulk heterojunction (BHJ) active layers are composed of at least two intermixed molecular species, a donor (D) and an acceptor (A), where exciton dissociation takes place at the D/A heterointerfaces via charge-transfer (CT) states. Commonly investigated BHJ organic solar cells (OSCs) and BHJ OPDs, however, offer a quite complicated microstructure when intermixing both phases [15]. The BHJ structure poses substantial challenges, including an enhanced likelihood of charge-carrier recombination and higher thermodynamic instability, which are detrimental to the device lifetime [15–17]. To address these critical limitations, significant research efforts have been directed toward devices featuring a simplified single-component (SC) architecture, in which the active layer is composed of a single functional organic semiconductor material [18–20]. In this architecture, typically D and A segments are covalently linked into distinct molecular segments within a single molecular structure, resulting in donor–acceptor small molecules as well as polymeric materials [21, 22]. For single-component OSCs (SC-OSCs), this results in cost reduction during the fabrication [20, 22], significantly improved morphological stability [22, 23], and higher reproducibility [19, 24]. Despite being less explored than their photovoltaic counterparts, emerging studies reveal that single-component OPDs (SC-OPDs) similarly capitalize on the advantages offered by their intrinsically simple device architecture [18, 25–31]. Therefore, this device layout provides a well-defined model system for probing the roles of interfacial effects in OPD performance. Rana et al. reported the efficient charge generation in chlorinated Subphthalocyanine (Cl_6-SubPc), identifying it as a suitable single-component material due to its high octupole moment [32]. The SubPc derivative Boron sub-2,3-naphthalocyanine chloride (SubNc) was investigated by Nikolis et al., [33] where the field-dependent charge carrier generation is explained by the built-in potential in SubNc-based devices. Interestingly, single-component OSC devices based on SubNc exhibited unusually high free charge generation without the assistance of a D/A heterojunction compared to other organic materials, possibly due to its higher dielectric constant [34]. These characteristics make SubNc a promising photoactive SC material for detection and enable dedicated investigation of interface effects.

In this study, SubNc-based single-component OPDs with a 3 nm thin Phenoxy-Subphthalocaynine (PhOSubPc) buffer layer (BL) to the organic electron transport layer (ETL) Bathophenanthroline (BPhen) are thoroughly investigated. The influence of the previously sparsely explored BPhen interface is explored, using several experimental techniques like ultra-sensitive EQE (us-EQE) measurement, ambient photoelectron spectroscopy (APS), and surface photovoltage (SPV). BPhen is a widely used evaporated ETL/hole-blocking layer (HBL), which was first mainly incorporated in organic light-emitting diodes (OLEDs) [35–38], but can nowadays be employed in organic or perovskite solar cells, and OPDs as well [18, 39, 40]. BPhen not only provides favorable injection/blocking energetics but also image-force-related effects that modify band bending at the contact [18, 35–39]. Furthermore, the use of top contacts, doping, and metal penetration can introduce vacuum-level displacements at the BPhen/metal interface, as well as activate transport sites and mid-gap states that enhance dark current [35–38]. Despite this, the specific influence of BPhen as an ETL on the energetic landscape and band bending at the immediate interface between organic (active) layers and BPhen in OPDs has not been systematically reported. Therefore, we incorporated a 3 nm buffer layer between the SubNc active layer and the BPhen ETL, which enables a systematic investigation of the interfacial effects while improving the OPD performance metrics. PhOSubPc is selected due to its structural analogy to SubNc, yet it possesses distinct electronic properties [33]. The BL serves as an interface probing layer to first investigate the direct SubNc/BPhen interface and, second, to establish a new PhOSubPc/BPhen interface to morphologically and energetically isolate and quantify the impact of the organic molecule on band alignment, device performance, and interfacial states. The optimized SubNc SC-OPD achieves highly competitive performance metrics such as peak EQE of 56 % at 0 V, an ultra-low J_D of $7.4 \cdot 10^{-12}$ A/cm^2 at −0.1 V, an ultra-low noise level of $4.3 \cdot 10^{-14}$ A/$\sqrt{Hz}$ at 0 V, and D^* of $1.7 \cdot 10^{12}$ Jones at 0 V (based on experimentally measured noise). Notably, J_D represents the lowest currently reported value, and D^* is among the highest reported to date for single-component OPDs [18, 25, 28, 30, 31, 41]. This study highlights the critical role of an ultra-thin organic buffer layer between the ETL and active layer in tailoring the interface energetics to achieve state of the art photodetection metrics in SC-OPDs.

2 | Results

2.1 | Investigated Device Structure of the SubNc SC-OPDs

As shown in Figure 1a, the investigated SC-OPDs are composed of SubNc as a photo-active material, which is sandwiched between a 5 nm thin 9,9-bis[4-(N,N-bis-biphenyl-4-yl-amino)phenyl]-9H-fluorene (BPAPF) & 30 nm p-doped BPAPF hole transport layer (HTL) on the ITO bottom contact, as well as a thin 3 nm PhO-SubPc buffer layer to the 5 nm ETL BPhen. The corresponding molecular structures are given in Figure 1c.

The energy levels (Figure 1d) show the highest occupied molecular orbital (HOMO) of all materials, which are measured using APS (Figure S1), and the lowest unoccupied molecular orbital (LUMO), which are estimated from the APS-measured HOMO and the optical bandgap determined by absorption spectra (Figure 1b).

2.2 | Optimization of the Layer Thickness and Interfaces

To achieve the optimal performance for the SubNc SC-OPD, the specific detectivity D^* needs to be maximized [14, 42]. D^*can be

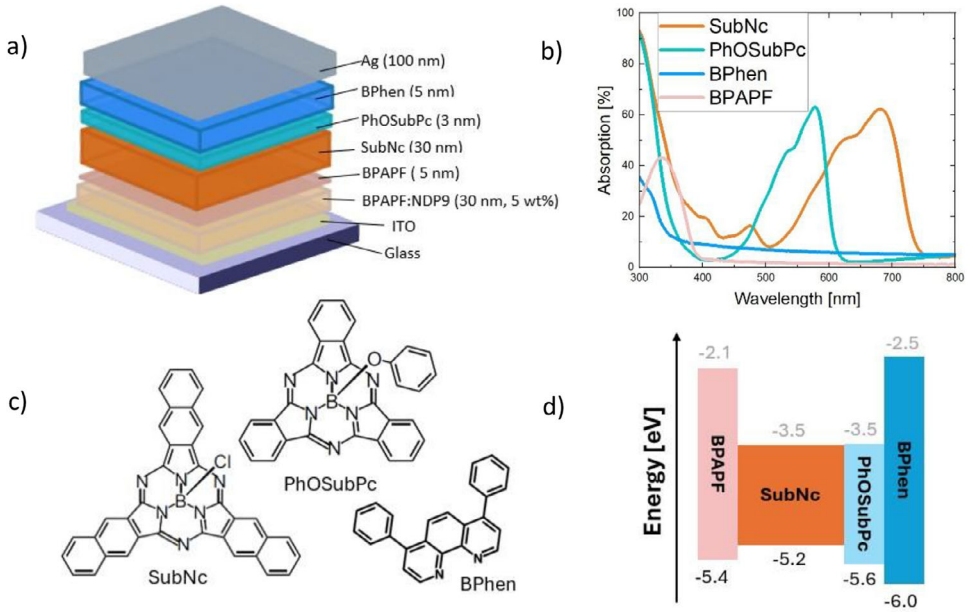

FIGURE 1 | (a) Schematic representation of the device stack structure, (b) measured absorption spectra of the active layer SubNc and the buffer layer PhOSubPc (30 nm thick films on glass substrates), (c) molecular structures of the active layer (SubNc), buffer layer (PhOSubPc), and ETL (BPhen), (d) energy diagram of the device stack. The HOMO levels are measured by APS, and the LUMO is estimated based on the HOMO and the optical bandgap determined by absorption spectra (Figure S1). For a) and d), the layer thicknesses are not on scale.

expressed by the following equation: [11]

$$D^* = \frac{e\lambda\sqrt{A \cdot \Delta f}}{hc} \cdot \frac{EQE}{i_{noise}} \tag{1}$$

where e is the elementary charge, λ is the wavelength, h stands for the Planck constant, c is the speed of light, $\Delta f$is the measurement bandwidth, and A is the device area. i_{noise} consists of several components:

$$i_{noise} = \sqrt{{i_{thermal}}^2 + {i_{shot}}^2 + {i_{1/f}}^2 + {i_{G-R}}^2 + \cdots} \approx \sqrt{{i_{thermal}}^2 + {i_{shot}}^2} \tag{2}$$

with

$$\sqrt{{i_{thermal}}^2 + {i_{shot}}^2} = \sqrt{\frac{4k_BT}{R_{shunt}} \cdot \Delta f + 2eJ_D \cdot \Delta f} \tag{3}$$

T is the temperature and k_B the Boltzmann constant. The noise contributions in equation 2 include the shot noise i_{shot} and the generation-recombination noise $i_{\text{G-B}}$, which are related to J_{D}; the thermal noise i_{thermal}, which is proportional to the shunt resistance R_{shunt} (see equation 3), and the so-called flicker noise ($i_{1/f}$), which is, in inorganic counterparts, commonly associated with charge carrier trapping and detrapping [11, 42, 43]. Assuming the shot and thermal noise components are the main noise contribution, equation 2 can be approximated by the expression on the right-hand side. The simplification typically underestimates the total noise, and therefore leads to an overestimation of D^*. Since a high D^* is the utmost goal, the EQE needs to be maximized while minimizing the dark current J_{D}. Therefore, the SubNc active layer thickness is varied between 12 and 50 nm to make the optimization, and the EQE (Figure 2a) and the current density—voltage (J–V) characteristic under illumination and in the dark are measured. The highest EQE of 65% at 710 nm, without external bias, is achieved at a SubNc thickness of 20 nm. The median of the box plots for the dark current density at higher reverse bias shows the lowest J_D values for 30 nm (J_{D} statistics at −2 V, Figure S3b). Furthermore, when calculating D^* based on thermal and shot noise at 0 V (equations 1 and 2), the highest value is obtained at 30 nm, with an EQE of 56% and a high R_{shunt} of $3.7 \cdot 10^{11}$ Ω/cm^2 at 0 V (Figure S3c).

To obtain insight into the thickness-dependence of the photocurrent and EQE behavior, we first employed a Kelvin probe and APS measurement to determine the Fermi and HOMO levels of SubNc films with different thicknesses. These measurements (Figure S3a and Table S1) confirm that the energetics are essentially independent of film thickness, thereby excluding energy-level variations as the origin of the observed EQE dependence. Then, SPV measurements were performed (Figure S2a,b) to further examine charge-generation and transport dynamics. SPV probes changes in surface potential under light illumination (here, broadband white light with an intensity of 20 mW/cm^2), which arise from the redistribution of photogenerated charge carriers, providing a sensitive means of assessing charge separation and recombination processes without a complete device architecture [44–46]. Figure S2a shows three SPV cycles for a partial device architecture of ITO/p-BPAPF & BPAPF/SubNc, measured as a function of SubNc thickness. All samples show a positive SPV response, indicating efficient extraction of the photogenerated holes by the p-BPAPF & BPAPF HTL and the accumulation of electrons at the SubNc surface. Compared with the 12 nm SubNc sample, the 25 nm sample shows much higher SPV response, which indicates enhanced photogeneration in thicker films and is consistent with the EQE results. For thicknesses above 25 nm, however, the SPV enhancement becomes negligible, suggesting that higher recombination losses might exist in thicker films and limit

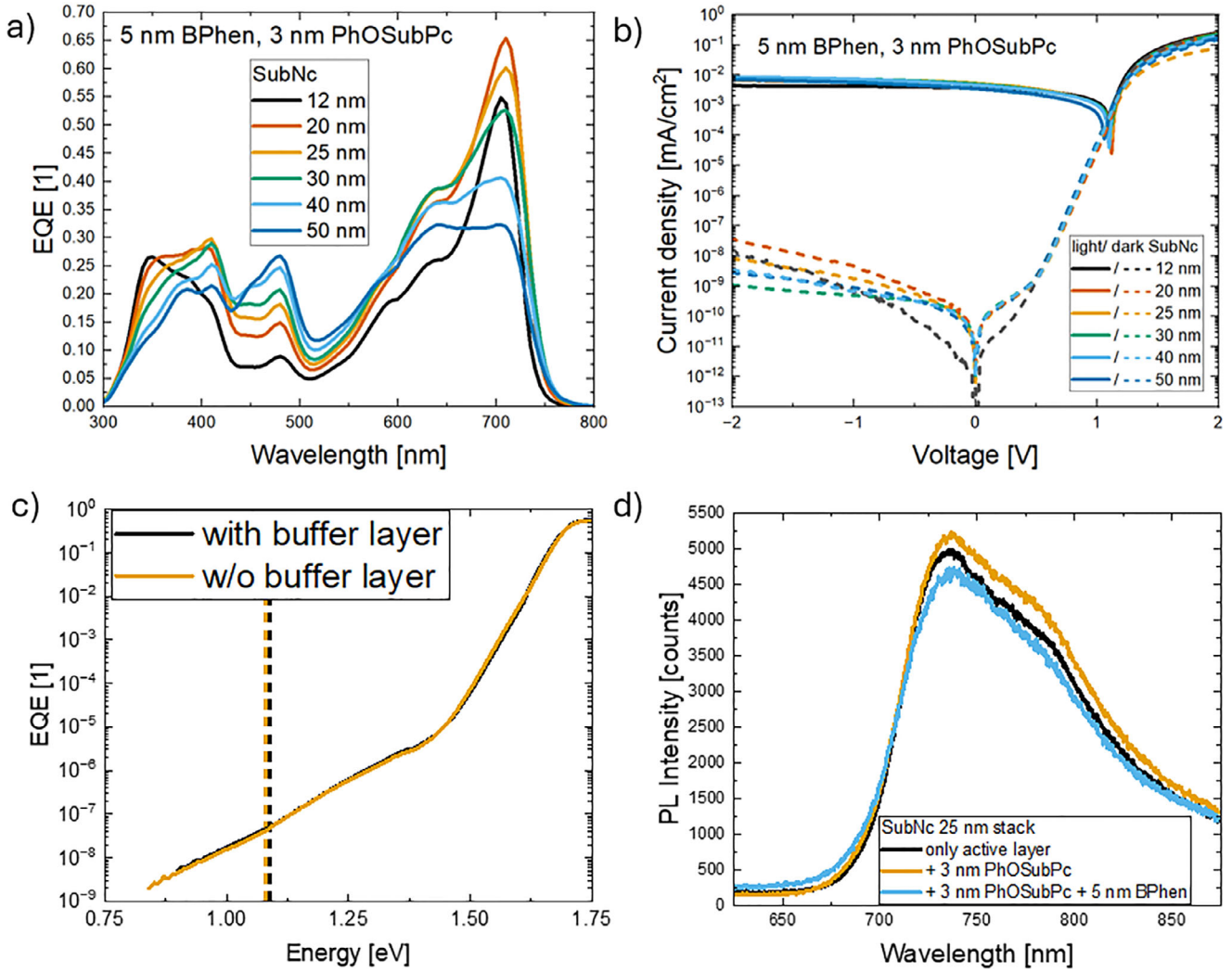

FIGURE 2 | Optimization of the active layer thickness: (a) the measured EQE spectra and (b) the measured *J*–*V* characteristic for the thickness series of 12–50 nm. Confirmation of single-component behavior: (c) measured us-EQE spectra for the optimized device thickness with and without 3 nm PhOSubPc buffer layer, where the dashed lines indicate the V_{OC}, and (d) the measured PL spectra for the added layers.

further increases in SPV and photocurrent. This is consistent with the decreasing EQE observed for thicknesses exceeding 25 nm. Figure S2b shows the normalized SPV response of the first illumination cycle in Figure S2a. The 25 and 30 nm films exhibit faster turn-on and turn-off dynamics, indicating faster charge generation and extraction in these devices, which also contributes to the high EQE. These improved response dynamics, combined with the thickness-dependent D^* analysis presented above, confirm that the 30 nm active layer provides optimized performance. Consequently, this thickness was selected for all the following evaluations.

2.3 | Investigating the Single-Component Nature of the Devices

To indicate the single-component character for the investigated devices, us-EQE measurements for 12–50 nm active layer thicknesses are performed (Figure S3d,e). The shape of the spectra suggests the absence of a CT feature for all thicknesses, indicating the SC character. Besides that, the absorption onset slope broadens with increasing SubNc thickness, due to the broadening of the absorption peak itself with increasing thickness, as shown by the simulated absorption in Figure S3f. Since the spectral shape of the sub-gap feature (intensity below 10^{-6} in Figure S3d,e) stays constant for all active layer thicknesses, the origin of it cannot be related to cavity enhancement [47].

Furthermore, the us-EQE spectra for the optimized thickness of 30 nm are shown in Figure 2c, to investigate the influence of the buffer layer explicitly on the SC behavior. Both spectra, with and without the buffer layer, resemble each other clearly and show no CT-related features, indicating the absence of a CT state between SubNc and the buffer layer. To further prove the absence of the CT state, we measure the activation energy E_A under illumination (Figure S4). For both devices, with and w/o buffer layer, we find a close agreement between the optical gap (E_{opt} of 1.71 eV, Table S2) of SubNc and the energy gap of the whole device (1.69 ± 0.02 eV and 1.71 ± 0.02 eV, respectively) [48]. For extra validation, photoluminescence (PL) measurements on the 25 nm SubNc films were carried out (Figure 2d). Compared with neat SubNc films, the introduction of the PhOSubPc buffer layer does

not result in PL quenching, indicating that charge generation does not originate from the active-layer/buffer-layer interface but rather occurs predominantly within the bulk of the SubNc layer. A modest PL quenching is observed upon further incorporation of BPhen on top of PhOSubPc, which is attributed to improved charge transport and thus reduced total radiative recombination. Collectively, the us-EQE, E_A, and PL measurements provide valid evidence to prove the single-component nature of the investigated material system, regardless of the buffer layer appearance.

2.4 | Photodetector Performance

To investigate the charge carrier generation and extraction mechanisms, bias-dependent EQE and PL measurements were carried out (Figure 3a,b). When applying a reverse bias of −2 V, the EQE increases from 56% (at 0 V) to 80% at the wavelength of 710 nm (Figure 3a). The increased EQE at reverse bias can result from improved charge generation, and/or charge transport. To further clarify the photocurrent increase, bias-dependent PL measurements are carried out, as seen in Figure 3b. The PL signal at 725 nm (1.71 eV) is strongly quenched upon applying a reverse bias. This observation indicates improved free charge generation assisted by the field-driven dissociation of the exciton, which is in agreement with the literature [33].

To benchmark the device's performance, we analyze the V_{oc} and I_{photo}/I_D relation, which was discussed in Gielen et al. according to the Shockley equation, the V_{oc} defines the ultimate limit of the I_{photo}/I_D ratio and thereby defines the lowest achievable J_D of the system [49]. Therefore, we first analyze the voltage losses of the optimized device from the us-EQE spectra (Figure 2c) and find the total voltage losses $e\Delta V_{loss}$ of 0.616 eV and a non-radiative voltage loss contribution ($e\Delta V_{non\text{-}rad}$) of 0.278 eV, which is in accordance with the literature (Table S2) [49, 59]. In Figure 3c, the V_{oc} is compared to the I_{photo}/I_D ratio at −0.1 V. The optimized device in this paper (indicated as an orange star in Figure 3c) stands out due to one of the largest I_{photo}/I_D ratios. However, according to the thermodynamic limit, we would expect a dark current that is approximately 10 orders of magnitude lower. Such a large discrepancy may arise from non-idealities, including shunt pathways, pinholes, electrically active trap states, or charge-carrier injection from the contacts [49]. To gain further insight into the origin of this behavior, the activation energy E_A of the dark current is extracted from temperature-dependent measurements using an Arrhenius analysis (Figure S5). The obtained E_A of 0.68 eV at −2 V is significantly smaller than the optical bandgap of 1.71 eV, which is consistent with (thermal) charge generation via intra-gap states rather than band-to-band processes [10]. In the literature, the reverse-bias dark current density is commonly reported to be dominated by thermally activated charge-generation processes via mid-gap trap states [10, 14, 55]. These measured defect-related states are therefore likely to represent one dominating factor in the pronounced deviation from the thermodynamic limit.

To evaluate the device performance of the optimized device, the specific detectivity needs to be calculated. Therefore, the noise spectral current density is measured for the frequency range of 0.5 – 2000 Hz, which shows a noise level at 172 Hz of $4.25 \cdot 10^{-14}$ $A/\sqrt{Hz}$ at 0 V and $8.84 \cdot 10^{-13}$ $A/\sqrt{Hz}$ at -2 V (Figure 3d). Looking at the measured spectra for 0 V (orange solid line), the flat curve at lower frequencies indicates no frequency dependence, while the spectra at reverse bias (blue solid line) increase at lower frequencies, which is associated with typical $1/f$ noise behavior [11, 14, 60]. While the fundamental origin of $1/f$ noise is still controversially discussed [61], it is commonly associated with charge carrier trapping and detrapping in inorganic counterparts [43]. We identify this same mechanism in our OPDs, supported by the presence of intra-gap states as shown in Figure S5. The dominance of this noise component at −2 V is attributed to the increased field-dependent band-bending under reverse bias, which significantly promotes the trapping-detrapping probability.

Calculating the specific detectivity at 710 nm based on the measured noise i_{noise}, D^* of $1.69 \cdot 10^{12}$ Jones at 0 V and $1.42 \cdot 10^{11}$ Jones at -2 V is obtained (Figure 3e). Comparing these values to the estimated D^* based on thermal and shot noise ($i_{thermal}$ & i_{shot}) at 710 nm (see equations 1 and 2), a two orders of magnitude higher value of D^* of $2.9 \cdot 10^{14}$ Jones (0 V) and D^* of $2.5 \cdot 10^{13}$ Jones (-2 V) are found, indicating that other noise contributions are also involved [11, 62]. To demonstrate the reproducibility of the dark current density and the shunt resistance values needed for the estimated D^* calculation, Figure 3f depicts the box plots for 11 measured devices. The average values (orange star) and the median values are $1.29 \cdot 10^{-11}$ and $5.37 \cdot 10^{-12}$ A/cm^2 for the J_D, and for the R_{shunt} $2.74 \cdot 10^{11}$ and $2.35 \cdot 10^{11}$ Ω/cm^2, respectively. Both figures of merit exhibit high degrees of clustering, indicating excellent reproducibility and confirming the exceptional dark-current characteristic.

To access the long-term stability of the investigated devices, EQE and J–V measurements were carried out after 10 months of storage under ambient laboratory conditions. The devices only show a minor EQE decrease: with a buffer layer, the EQE decreased from 56% to 52%, and without the buffer layer, the EQE decreased from 54% to 50%. The J–V spectra under illumination show a stable V_{OC}, and the dark current density remains essentially unchanged (Figure S6b), indicating minimal degradation of the devices. These results confirm the robust long-term operational stability of the SubNc SC-OPDs.

2.5 | Investigating the Impact of Interlayers

To understand the excellent performance, we aim to unveil the role of the organic functional interlayers, specifically a 3 nm PhOSubPc buffer layer and a 5 nm BPhen ETL (organic layer build-up can be seen in Figure 4a). Figure 4b shows the SPV response of a series of partial devices based on the architecture of the full device. Compared with the ITO/HTL/SubNc sequence, introducing PhOSubPc results in a modest SPV increase of ∼10 meV, whereas further introduction of BPhen results in a more pronounced enhancement of ∼40 meV. This marginal magnitude improvement indicates efficient electron extraction from SubNc into the buffer layer or ETL, thereby suppressing recombination loss and strengthening the overall SPV response. This indicates the effective stack layout with respect to the SPV response. From the normalized SPV data (Figure 4c), after light turn-off, a slower decay in the second-phase is observed in the presence of BPhen. Because these measurements are performed on partial devices without a top electrode, electrons transferred into the BPhen layer

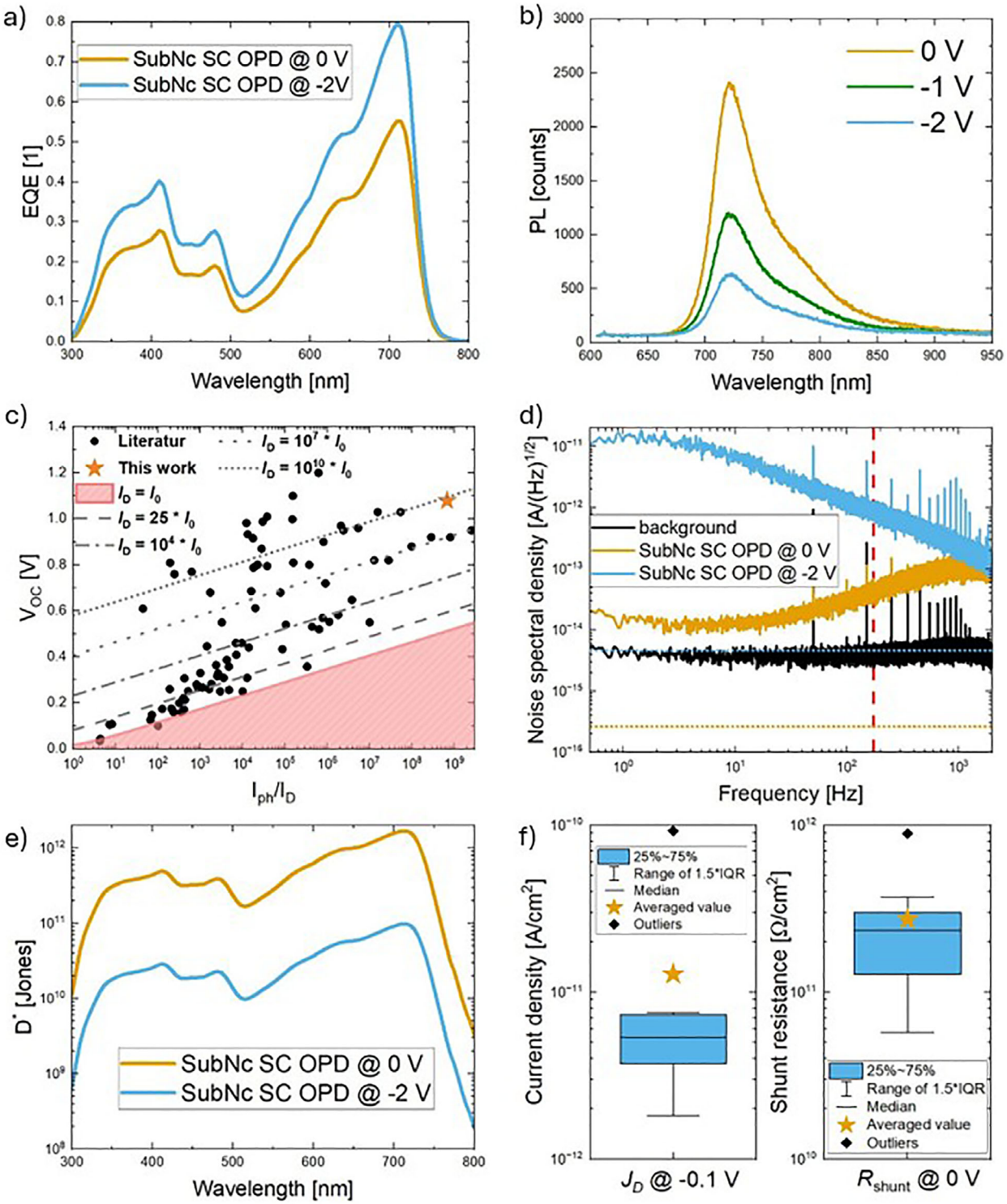

FIGURE 3 | (a) The measured EQE of the optimized SubNc SC-OPD, (b) shows the measured PL intensity, at zero bias (orange), −1 V in green (for Figure 3b), and reverse bias (−2 V, blue), respectively. (c) depicts the calculated ratio of I_{photo} to I_D extracted at −0.1 V to the measured V_{OC}. The plot is inspired by Gielen et al. [49]. and has been updated here. The orange star represents this work, while the black symbols depict reported OPDs, mainly BHJs (all values can be found in Table S3). The red solid line indicates the lower thermodynamic limit of J_D. [5, 10, 18, 32, 41, 49–58] d) shows the measured spectral noise current density of the background and the SubNc SC-OPDs at 0 (orange) and −2 V (blue), where the vertical red dashed line indicates the frequency of 172 Hz, measured, and at which the noise level was extracted to calculate the specific detectivity D*. The horizontal orange and blue dotted lines symbolize the calculated shot and thermal noise at 0 and –2 V, respectively, and e) depicts the specific detectivity D* based on the measured noise characteristic at 172 Hz at zero bias (orange). f) shows box plots of 11 investigated devices to prove the record low dark current density at −0.1 V (left axis and box) as well as the high shunt resistance at zero bias (right axis and plot). The orange star represents the averaged value, and the blue box represents the range of 1.5*interquartile range (IQR).

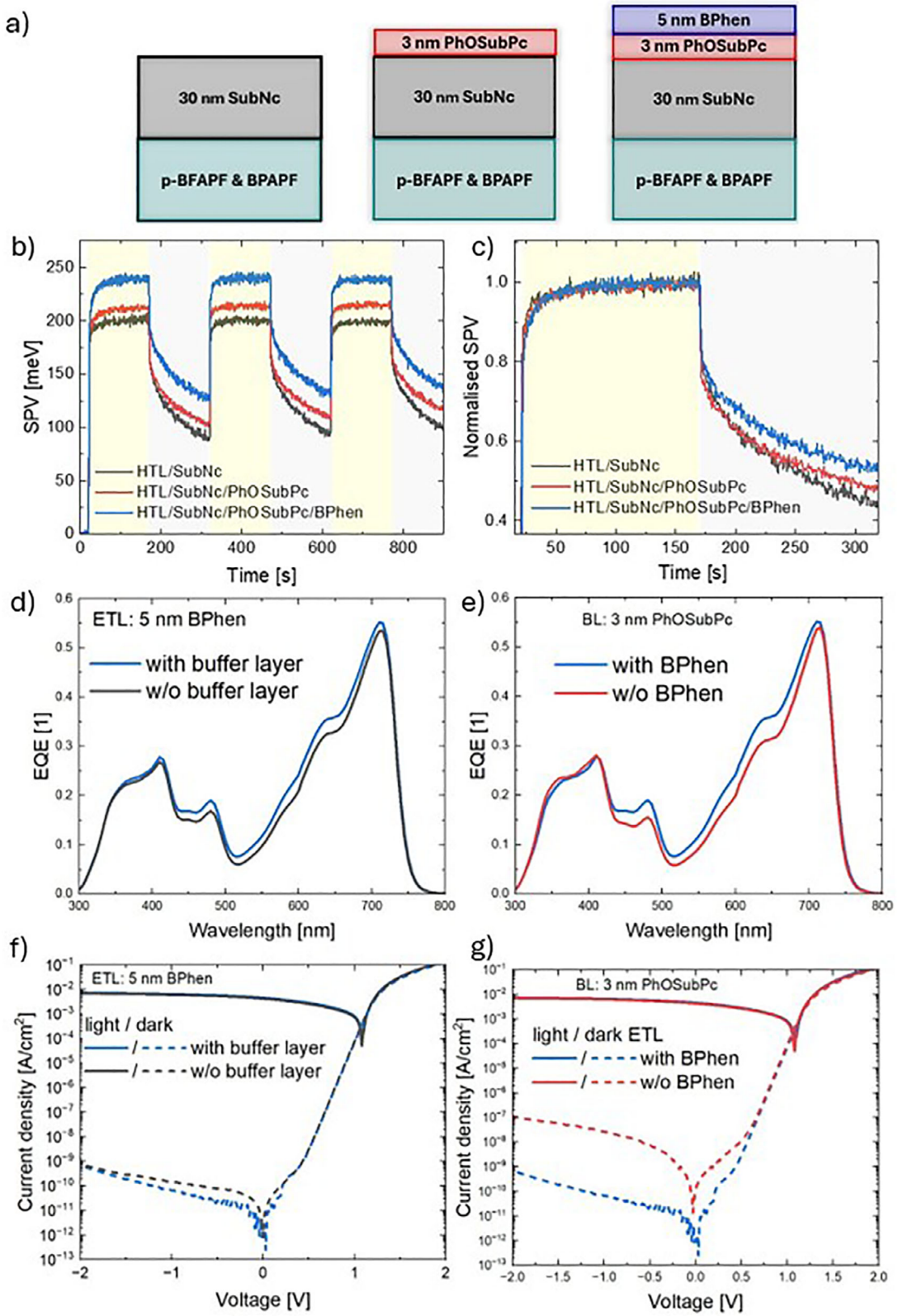

FIGURE 4 | (a) Sample structure diagrams, where the layer thicknesses are not on scale, (b) surface photovoltage plot, (c) normalized surface photovoltage plot, (d,e) the EQE, as well as (f,g) the *J*–*V* spectra under illuminated and dark conditions for the SubNc SC-OPD with and without 3 nm PhOSubPc buffer layer (blue, black), as well as with and without BPhen as ETL (blue, red).

cannot be efficiently extracted and therefore accumulate and become trapped within the ETL. This charge retention prolongs recombination dynamics and leads to the observed slower decay. Similar trends are observed across samples with the same stack but varied active layer thickness (see Figure S7), which confirms the reproducibility of the measured results.

We also measured the device EQE (Figure 4d,e; bias dependency shown in Figure S8) and *J–V* with and without the PhOSubPc buffer layer and BPhen ETL (Figure 4f,g), to understand the role of the interlayers on a device level. A slight enhancement of approximately 2–3%pt. across 420–700 nm is observed upon introducing PhOSubPc, increasing further to 2–4%pt. with the additional BPhen layer. These EQE gain leads to an increase in the short-circuit current J_{SC} of about 7% when adding the ETL and 9% when adding the BL and the ETL. Despite these improvements, the overall EQE spectra with and without the buffer layer or ETL still resemble each other, which indicates that the production of free charge carriers predominantly happens in the bulk of the active layer, in agreement with the SC characteristic as shown in Figure 2c,d. Beyond these modest photoresponse differences, the dark current density is more strongly affected, with the BPhen ETL suppressing J_D by over two orders of magnitude. This striking reduction originates from the deep HOMO of BPhen, which provides strong hole-blocking capability to prevent unfavorable hole injection in combination with improved electron extraction [63, 64]. The SPV trends align well with the device-level measurements, underscoring the crucial role of these organic interlayers in governing the photophysical behavior and overall device performance.

Since the decrease of J_D can have several origins, like shunts which can originate due to non-ideal surface smoothness, atomic force microscopy (AFM), and grazing-incidence wide-angle X-ray scattering (GIWAXS) measurements were performed to investigate the morphology. Both the neat 30 nm thick SubNc (Figure S9a) and a 30 nm thick PhOSubPc film (Figure S9b) exhibit a low root-mean-square (RMS) roughness of 2.2 and 1.7 nm, respectively, in the AFM. While the features of SubNc transition more rapidly, the ones of PhOSubPc merge smoothly into one another. Depositing a 3 nm PhOSubPc layer on 30 nm SubNc yields a similar morphology and RMS roughness (2.0 nm; Figure S9c), confirming that this thickness is sufficient for uniform coverage. Upon thermal evaporation of 5 nm BPhen onto the buffer and active layer, the surface roughness is further reduced to 1.1 nm (Figure S9d), creating a smooth surface. GIWAXS measurements confirm that SubNc and PhOSubPc films are amorphous (Figure S10a–c), showing no additional diffraction features beyond the substrate background (Figure S10f). In contrast, the addition of BPhen results in distinct polycrystalline diffraction rings (Figure S10d), which can be fitted by an orthorhombic unit cell with $a = 7.16$ Å^{-1}, $b = 10.82$ Å^{-1}, $c = 21.10$ Å^{-1}. This unit cell is almost identical to the one reported in the literature for single crystals of BPhen [65].

To investigate the influence of the buffer layer on the frequency response of the devices, the cutoff frequency ($f_{-3\,dB}$) was determined (Figure S11a–d). Both devices—with and without the buffer layer—show a high $f_{-3\,dB}$ of 101 kHz at 0 V and a slightly higher one at -2 V (135 and 115 kHz). In line with the slightly higher f_{-3db} at -2 V for devices with a buffer layer, we also observed a moderately faster rise and fall times [57] of 3.37/3.12 μ*s* (with BL) and 4.64/3.99 μ*s* (w/o BL) (see Table S4). Besides that, the linear dynamic range (*LDR*) for both SubNc SC-OPDs is very high, with the device with a buffer layer achieving an LDR of 164.4 dB, surpassing that without one (147.5 dB). This corresponds with the very low J_D of both devices. With slopes of ∼0.99 for both devices, the values are very close to unity (Figure S11e,f).

2.6 | Energetic Landscape of the Interlayers

To further elucidate the mechanism by which PhOSubPc and BPhen function as a buffer layer and ETL to enhance electron extraction, we also considered the corresponding energetic landscape. It is worth noting that HOMO levels reported in the literature vary depending on the characterization technique, such as ultraviolet photoelectron spectroscopy (UPS), cyclic voltammetry (CV), etc. Nevertheless, the HOMO values of SubNc (−5.20 eV), PhOSubPc (−5.55 eV), and BPhen (−6.00 eV) measured by APS in this work are largely consistent with previously reported ranges [33, 66–69].

Figure 5a shows the APS spectra of neat SubNc, neat BPhen, and the bilayer SubNc (30 nm)/BPhen (5 nm). Interestingly, the measured HOMO of the SubNc/BPhen stack is −5.25 eV, which is very close to the intrinsic SubNc HOMO. Several factors may account for this observation. 1) Incomplete or inhomogeneous BPhen coverage: if the BPhen layer does not fully cover the SubNc surface, regions of exposed SubNc would dominate the APS signal within the limited probing depth of the technique (a few nanometers). 2) Intermixing at the interface: partial interdiffusion of BPhen into SubNc during deposition could lead APS to probe a mixed region with a shallower apparent HOMO. 3) Thickness-dependent BPhen energetics: although unlikely, variations in the HOMO at ultrathin thicknesses cannot be fully excluded. However, existing literature strongly suggests that the BPhen HOMO is thickness-independent. For example, Olthof et al. [35] reported a HOMO of −6.38 eV for 5 nm BPhen (same thickness as our work) deposited on α-NPD:Ir(MDQ)$_2$(acac) and BPhen:Cs, measured by UPS. Taken together, these considerations indicate that the unusually shallow HOMO observed for the SubNc/BPhen stack most likely originates from intermixing and/or incomplete surface coverage rather than intrinsic energetic shifts in BPhen. This suggests that direct deposition of BPhen onto SubNc does not provide an optimal interfacial morphology and energetics for device fabrication.

Figure 5b,c illustrates the impact of introducing a 3 nm PhOSubPc interlayer on the interfacial energetics. Figure 5b suggests that the measured HOMO (−5.50 eV) of SubNc (30 nm)/PhOSubPc (3 nm) closely matches that of neat PhOSubPc (−5.55 eV) even at this ultrathin thickness. This behavior indicates that, unlike the SubNc/BPhen interface, PhOSubPc forms a uniform layer that effectively covers the SubNc surface, in agreement with AFM results. Upon further deposition of BPhen (Figure 5c), the measured HOMO shifts to −5.83 eV, approaching the intrinsic BPhen HOMO level and markedly deeper than the much shallower HOMO observed for the direct SubNc/BPhen contact (Figure 5a). The slightly shallower value relative to neat BPhen in Figure 5c can be attributed to polarization or screening effects induced by the underlying PhOSubPc layer [70]. This observation

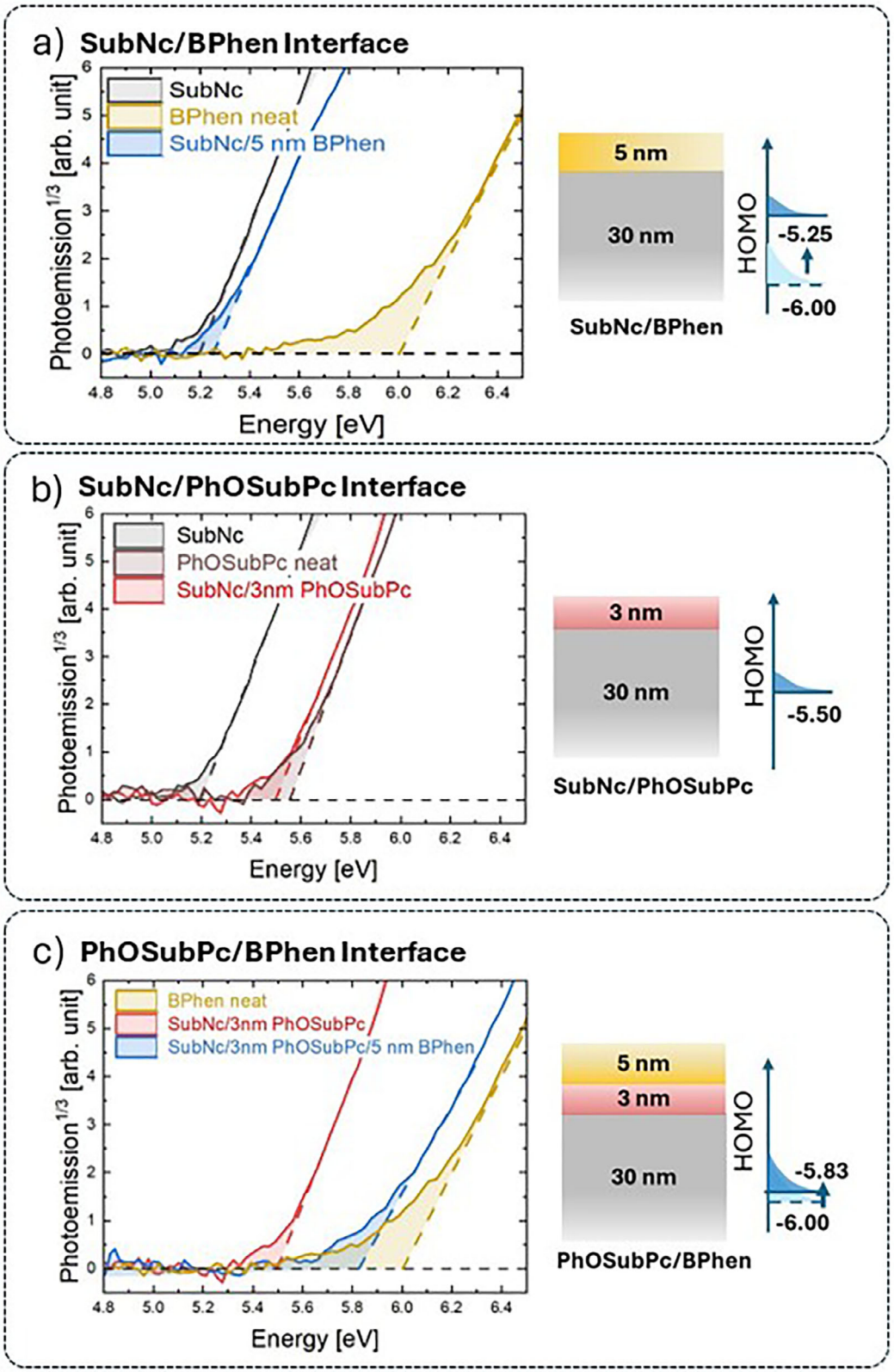

FIGURE 5 | Ambient photoemission spectra and the corresponding energetic diagrams. The dotted lines are used to fit HOMO levels, and the shadowed area indicates the density of states (DOS) within the bandgap. The HOMO levels shown in the right-hand side diagrams are derived from the left-hand side APS measurement results. Sample thicknesses are labelled in energetic diagrams. The layer thicknesses are not on scale.

demonstrates that the PhOSubPc interlayer effectively covers the SubNc surface and electronically decouples SubNc from BPhen. This decoupling is likely facilitated by the bulky phenoxy substituents in PhOSubPc, which inhibit intermixing and thereby preserve the intrinsic energetics of the individual layers. Consequently, insertion of the PhOSubPc buffer layer increases the hole injection barrier at the interface by deepening the HOMO level, thereby suppressing the J_D.

To further examine the buffer layer coverage continuity, we performed a thickness-dependent APS study, varying the PhOSubPc buffer layer thickness from 0 to 6 nm (Figure S12). When BPhen is deposited directly on the active layer (0 nm buffer layer, dark green), the measured HOMO shifts strongly toward that of SubNc, as shown in Figure 5a. In contrast, inserting a 3 nm PhOSubPc buffer layer between SubNc and BPhen yields a HOMO level close to that of intrinsic BPhen (Figure 5c). Further increasing the PhOSubPc thickness to 6 nm produces no additional change in the BPhen HOMO level (medium and light green in Figure S12). From 3 to 6 nm PhOSubPc, this energetic thickness-independent behavior proves that a 3 nm PhOSubPc layer is sufficient to form a largely continuous and smooth layer to effectively screen the SubNc layer and to suppress interfacial intermixing between SubNc and BPhen.

In addition, pronounced tail states are observed in the APS spectra of both thick neat BPhen films and SubNc/PhOSubPc/BPhen stacks, indicating a substantial density of states within the bandgap that is intrinsic to BPhen and preserved upon integration into the device stack. In our device structure, these sub-gap states near the HOMO edge can be associated with trap states that could contribute to the trap-mediated J_D (see Figure S5). To evaluate the interfacial trap density, we further compared the integrated spectral intensity below the photoemission threshold (shadowed region in Figure 5; integration results shown in Figure S13) [50, 71, 72]. From this analysis, the relative trap-state intensity for the SubNc/PhOSubPc/BPhen stack is higher than that of the SubNc/BPhen stack. These APS results suggest that the primary effect of the PhOSubPc interlayer is to increase the hole injection barrier instead of reducing the interfacial trap density. Importantly, the presence of these substantial intragap states near the LUMO edge could also be beneficial to support electron hopping through the ETL, facilitating efficient electron conduction [73]. The work functions of all relevant samples were also measured and summarized in Table S5. A pronounced work function shift of approximately 170 meV is observed after depositing BPhen on top of SubNc/PhOSubPc, corresponding to a vacuum level shift induced by an interface dipole at the PhOSubPC/BPhen interface. This interface dipole is favorable for electron extraction into the BPhen layer and consistent with the observed reduction in dark current density.

The combined introduction of PhOSubPc and BPhen plays an important role in establishing a favorable interfacial energetic landscape for efficient electron extraction. PhOSubPc acts as an electronically decoupling templating layer that suppresses SubNc/BPhen intermixing or inhomogeneous coverage and preserves the intrinsic energy levels of the adjacent layers, which allows us to disentangle the SubNc/BPhen interaction. Therefore, PhOSubPc acts also energetically as a functional buffer layer. BPhen, in turn, provides a high density of intragap states that facilitate electron transport and establish an interfacial dipole that induces downward band bending for electron transport. Together, these interlayers reduce recombination losses, enhance carrier extraction, and ultimately enable the superior device performance observed in the optimized single-component OPDs.

3 | Conclusions

In conclusion, we investigated a SubNc single-component OPD that incorporates a 3 nm PhOSubPc interfacial layer to systematically probe the interaction between the SubNc absorber and the BPhen ETL. This ultrathin layer acts as an energetic spacer, effectively isolating SubNc from BPhen while simultaneously providing a modest performance enhancement. By optimizing the SubNc layer thickness, we identified 30 nm as the optimal active-layer thickness, offering the best compromise between fast turn-on and turn-off dynamics, high EQE, and ultra-low dark current. APS measurements on this optimized device further confirm the energetic decoupling of SubNc and BPhen, enabling a clearer understanding of interfacial effects in single-component OPDs.

The resulting SubNc SC-OPD achieves an EQE of 56% at 0 V, an ultra-low J_D of $7.4 \cdot 10^{-12}$ A/cm^2 at –0.1 V, and a D^* of $1.69 \cdot 10^{12}$ Jones at 0 V (based on measured noise). The measured J_D is the lowest value reported to date for single-component OPDs, and the corresponding D^* ranks among the highest values for single-component devices in the field. Together, these results demonstrate that simplified single-component architectures can serve not only as useful model systems for disentangling energetic, morphological, and physical processes but also as a pathway to high-performance organic photodetectors.

4 | Experimental Methods

4.1 | Materials and Substrates

Glass substrates with 90 nm prestructured ITO were purchased from Suzhou ShangYang Solar Technology Co., Ltd. Bathophenanthroline; 4,7-diphenyl-1,10-phenanthroline (BPhen), and the active layer Boron sub-2,3-naphthalocyanine chloride (SubNc) were purchased from Luminescence Technology Corp., Taiwan. 9,9-bis[4-(N,N-bis-biphenyl-4-yl-amino)phenyl]-9H-fluorene (BPAPF) was bought from BLD Pharmatech GmbH, Germany. Phenoxy-Subphthalocaynine (PhOSubPc) was fabricated at the IAPP Dresden, and NDP9 was purchased from Novaled GmbH, Germany. Silver (Ag) was purchased from Kurt J. Lesker, USA. All organic materials were purified 1–2 times via thermal sublimation.

4.2 | Device Preparation

All devices were thermally evaporated in a vacuum chamber (Kurt J. Lesker, UK) with a base pressure below 10^{-7} mbar. The effective active area of 6.44 mm^2 is defined by the overlap of the bottom and top contacts. Before fabrication, the glass substrates with pre-structured ITO were cleaned with NMP solvent, deionized water, and ethanol. For the doped hole transport layer

(HTL), 5 wt% NDP9 was used. After processing, all devices were encapsulated by gluing transparent glass onto the device's top surface using a UV-cured epoxy resin (Nagase ChemteX XNR 5570, Japan). A moisture getter (Dynic Ltd., UK) was inserted between the top contact and the glass to prevent degradation.

4.3 | UV–Vis Absorption

The Reflection R and transmission T spectra were measured using a laboratory UV–vis–NIR spectrometer (Shimadzu SolidSpec-3700, Japan) in an integrating sphere. R and T of 30 nm thick films of neat SubNc and PhOSubPc on a glass substrate were measured. The absorption of BPhen and BPAPF was measured by S. Olthof and S. Buchholtz, respectively, with 30 nm BPhen or BPAPF on a quartz substrate. The depicted absorption A was calculated by: $A = 100\% - R - T$.

4.4 | External Quantum Efficiency

A xenon lamp (Ushio UXL-150SO, Japan) with the light intensity of 150 W was used as a light source. This light was chopped at a frequency of 172 Hz and led into a monochromator from Newport Cornerstone 260 1/4m, USA. Afterwards, the photocurrent was amplified using an amplifier from Stanford Research SR570, USA, and fed to a lock-in amplifier (Signal Recovery SR 7265, USA). The photoactive area of 2.997 mm^2 was defined using a mask. A silicon diode (Hamamatsu Photonics S1337, Japan) was utilized for calibration.

4.5 | Current–Voltage Characteristics

Illuminated current–voltage measurements were carried out under ambient conditions using a 300 W xenon lamp (Ushio UXL-300D-0, Japan) integrated into a sun simulator (Solar Light Co. Sunlight Simulator 16S-003-300-AM1.5, USA). It was operated at 100 mW cm^{-2}. To calibrate the light intensity, a silicon photodiode (Hamamatsu Photonics S1337, Japan) was used. No mismatch correction was applied to ensure accurate 1-sun conditions. Voltage-dependent photocurrent was recorded using a source-measure unit (Keithley Instruments SMU 2400, USA). For the dark J–V measurements, a highly sensitive source-measure unit (Keithley Instruments SMU 2635A, USA) was connected. Holding times up to 500 s were applied to erase capacitive charge effects. All measurements were run via the SweepMe! software (sweepme.net).

4.6 | Ultra-Sensitive External Quantum Efficiency

The ultra-sensitive *EQE* measurements were performed in ambient conditions using light chopped at 172 Hz from a 250 W halogen lamp (OSRAM HLX 64657, Germany). The light was coupled into a double monochromator from Quantum Design GmbH MSHD-300A, Germany. Afterwards, the monochromatic light was focused on the investigated device, and its generated photocurrent was measured under short-circuit conditions. A current-voltage preamplifier (Stanford Research Systems SR 570, USA) was used to amplify and then fed the signal to a lock-in amplifier (Stanford Research Systems SR830, USA) with a time constant of up to 3 s. To calculate the *EQE* by dividing the photocurrent of the OPD by it, the flux of incident photons was measured using a calibrated Si (Thorlabs FDS100-CAL, USA) and an InGaAs photodiode (Hamamatsu Photonics G12183_020K, Japan). The measurement software SweepMe! (sweep-me.net) was used to control the setup.

4.7 | Suns-V_{oc}

Temperature- and light-dependent J–V measurements are performed in a customized cryostat composed of a vacuum chamber (1 mbar air pressure), water cooling, and a white LED (MWWHLP1, Thorlabs GmbH, Germany), mounted on the cryostat. A BelektroniG Hat Control-K10 temperature controller was used. A very sensitive SMU (Keithley 2635A, Textronix Inc., USA) is connected to the sample in the cryostat. The different light intensities were applied using the LED mentioned above, which was connected to a dual-channel SMU (Keithley 2602A, Textronix Inc., USA). The setup was controlled by the measurement software SweepMe! (sweep-me.net).

4.8 | Noise Measurements

The noise current is measured by connecting a very low noise current-voltage preamplifier (26DHPCA-200, FEMTO Messtechnik GmbH, Germany) to the device, placed in a light isolating and electric shielding box. The internal voltage supply enables bias-dependent noise measurements. The signal was recorded by a high-speed, low-noise oscilloscope from Agilent 33600A Series, USA, with a low-pass electrical filter with $\leq$2 kHz passband (EF112, Thorlabs Inc., USA) and a sampling frequency that was at least double the cut-off frequency of the low-pass filter.

4.9 | Atomic force microscopy

The atomic force microscopy (AFM) measurements were performed in tapping mode using a Bruker Dimension Icon tool operated with ScanAsyst. A Bruker RTESPA-150 probe was employed. The software Gwyddion was used to post-process the data.

4.10 | Optical Simulation

The optical simulations were performed with the open-source Python program "Simojio" [74] based on the transfer matrix model (TMM) implemented by S. Byrnes [75].

4.11 | Grazing-Incidence Wide-Angle X-Ray Scattering (GIWAXS)

The GIWAXS measurements were performed at beamline ID10-SURF at the European Synchrotron Radiation Facility (ESRF), France. The photon beam energy was 22.5 keV, and a Dectris Eiger2 4 M area detector was used to record the scattering images. The sample-to-detector distance was 352.4 mm and was

verified using a lanthanum hexaboride standard. The beam had dimensions of 10 μm vertically and 60 μm horizontally, and all measurements were performed with an incidence angle of 0.04°. The samples were placed into a helium-filled chamber with Kapton windows and then exposed for 30 s to the beam. All the scattering data were analyzed with WxDiff [76].

4.12 | Photoluminescence

Photoluminescence (PL) spectra were recorded on a Renishaw in Via Raman microscope in backscattering geometry using a 514 nm argon-ion laser (ModuLaser). Film samples were held in a customized Linkam chamber under continuous nitrogen flow to minimize degradation. Device PL was measured under applied reverse bias in a nitrogen-filled chamber. Laser power, exposure time, and accumulation numbers were optimized to maximize signal-to-noise while avoiding sample damage.

4.13 | Energetic Measurements and Surface Photovoltage

APS, SPV, and dark work function (DWF) measurements were performed using a KP Technology APS04 system. DWF was measured first, followed by Surface Photovoltage (SPV), and then APS, to minimize UV-induced degradation. DWF and SPV were measured with a 2 mm Au Kelvin probe (off-null system) calibrated against the contact potential difference (CPD) and APS response of a freshly cleaned Ag reference. SPV employed broadband illumination (400–800 nm, 0.2 suns) from a quartz tungsten lamp, with simultaneous CPD monitoring at 0.8 Hz. APS spectra were collected using a monochromated UV lamp with photon energies from 4.5 to 6.8 eV. Photogenerated electrons were collected with the Kelvin probe biased at 10 V. HOMO levels were extracted by fitting the linear region of the cube root of the photoemission current.

4.14 | Transient Photocurrent and Frequency Response

Transient photocurrent (TPC) was performed with a 405 nm laser system (CUBE 405–50C, Coherent Corp., USA). A beam expander (ZBE22, Thorlabs GmbH, Germany) extends the illumination spot to ensure uniform intensity throughout the entire pixel area. The laser was modulated externally and digitally by a high-frequency waveform generator (SDG6052X, Siglent Technologies GmbH, Germany). The electrical output from the device was amplified by a transimpedance amplifier (DHPCA-100, Femto Messtechnik GmbH, Germany) before being fed into the oscilloscope (SDS1204X-E, Siglent Technologies GmbH, Germany). The frequency response was obtained by performing a Fourier transform of the TPC signal acquired at the corresponding frequencies. $f_{-3\,dB}$ is obtained by subsequent normalization.

4.15 | Linear Dynamic Range

A 660 nm LED (Thorlabs M660L4, USA), which was operated using an LED driver (Thorlabs DC2200, USA) and modulated at 172 Hz was used to illuminate the sample. A series of neutral density filters, purchased from Thorlabs, USA were used to gain a wide range of light intensity. The sample was placed into an electrically shielded box to decrease external noise sources during the measurement. Afterwards, the photocurrent was preamplified (FEMTO Messtechnik GmbH DLPCA-200, Germany) and fed into a lock-in amplifier from Stanford Research Systems SR865A, USA. To calibrate the signal, a silicon diode (Thorlabs SM05PD3A, USA) was measured as well. The setup was controlled by the measurement software SweepMe! (sweep-me.net).

Acknowledgements

A.K. acknowledges the DFG project DANCE (LE 747/74-1) as well as the Graduiertenakademie for the funding of the research stay at the Imperial College London (PSP-Element: F-010000-702-5B1-2330000 f). J.B., J.W., and L.C.W. gratefully acknowledge funding from the Federal Ministry of Research, Technology, and Space (BMFTR) as part of the project to establish the German Centre for Astrophysics (03WSP1745), and L.C.W. acknowledges the Graduate Academy project 2767 (GRK 2767). F.K. acknowledges the SAB-Project NDOT (Neuartige n-Dotanden für OPV und OLED, Project no. 100716679). A-L.H. thanks the Koselleck-project from the DFG (456344071). T.Z. acknowledges the SAB funding EFRE, and OPTICUS (Project number: 100770861). M.H and S.C.B.M acknowledge the European Synchrotron Radiation Facility (ESRF) for the provision of synchrotron radiation facilities, and we would like to thank Dr. Oleg Konovalov for assistance and support in using beamline ID10-SURF. We would like to thank Vojtech Millek and Ertürk Enver Yildirim for their help with the GIWAXS measurements. J.-S. Kim acknowledges UKRI EPSRC ATIP Programme Grant (EP/T028513/1) in UK, and the Ewha Global Excellence Program.

Open access funding enabled and organized by Projekt DEAL.

Conflicts of Interest

The authors declare no conflicts of interest.

Data Availability Statement

The data that support the findings of this study are available from the corresponding author upon reasonable request.

References

1. F. Zhuge, Z. Zheng, P. Luo, et al., "Nanostructured Materials and Architectures for Advanced Infrared Photodetection," *Advanced Materials Technologies* 2 (2017): 1700005.

2. H. T. Chandran, J. Huang, H. Xia, et al., "Beyond Silicon: Toward Sustainable, NIR-II, and Conformable Organic Photodiodes," *Advanced Energy Materials* 16 (2026): 04357.

3. M. Long, P. Wang, H. Fang, and W. Hu, "Progress, Challenges, and Opportunities for 2D Material Based Photodetectors," *Advanced Functional Materials* 29 (2019): 1803807.

4. P. Martyniuk, J. Antoszewski, M. Martyniuk, L. Faraone, and A. Rogalski, "New Concepts in Infrared Photodetector Designs," *Applied Physics Reviews* 1 (2014): 041102.

5. B. Park, J. Jung, D.-H. Lim, et al., "Significant Dark Current Suppression in Organic Photodetectors Using Side Chain Fluorination of Conjugated Polymer," *Advanced Functional Materials* 32 (2022): 2108026.

6. J. Huang, J. Lee, J. Vollbrecht, et al., "A High-Performance Solution-Processed Organic Photodetector for Near-Infrared Sensing," *Advanced Materials* 32 (2020): 1906027.

7. P. C. Y. Chow and T. Someya, "Organic Photodetectors for Next-Generation Wearable Electronics," *Advanced Materials* 32 (2020): 1902045.

8. D. Yang and D. Ma, "Development of Organic Semiconductor Photodetectors: from Mechanism to Applications," *Advanced Optical Materials* 7 (2019): 1800522.

9. H. Ren, J.-D. Chen, Y.-Q. Li, and J.-X. Tang, "Recent Progress in Organic Photodetectors and Their Applications," *Advanced Science* 8 (2021): 2002418.

10. O. J. Sandberg, C. Kaiser, S. Zeiske, et al., "Mid-gap Trap State-Mediated Dark Current in Organic Photodiodes," *Nature Photonics* 17 (2023): 368–374.

11. Y. Wang, J. Kublitski, S. Xing, et al., "Narrowband Organic Photodetectors—Towards Miniaturized, Spectroscopic Sensing," *Materials Horizons* 9 (2022): 220–251.

12. Y. Kim, C. Eon Park, and D. Sung Chung, "Interface Engineering of a Highly Sensitive Solution Processed Organic Photodiode," *Physical Chemistry Chemical Physics* 16 (2014): 18472.

13. T. Li, Z. Chen, Y. Wang, et al., "Materials for Interfaces in Organic Solar Cells and Photodetectors," *ACS Applied Materials & Interfaces* 12 (2020): 3301–3326.

14. J. Kublitski, A. Hofacker, B. K. Boroujeni, et al., "Reverse Dark Current in Organic Photodetectors and the Major Role of Traps as Source of Noise," *Nature Communications* 12 (2021): 551.

15. M. Riede, D. Spoltore, and K. Leo, "Organic Solar Cells—The Path to Commercial Success," *Advanced Energy Materials* 11 (2021): 2002653.

16. A. Wadsworth, Z. Hamid, J. Kosco, N. Gasparini, and I. McCulloch, "The Bulk Heterojunction in Organic Photovoltaic, Photodetector, and Photocatalytic Applications," *Advanced Materials* 32 (2020): 2001763.

17. S. Zeiske, O. J. Sandberg, N. Zarrabi, W. Li, P. Meredith, and A. Armin, "Direct Observation of Trap-assisted Recombination in Organic Photovoltaic Devices," *Nature Communications* 12 (2021): 3603.

18. J. Wolansky, C. Hoffmann, M. Panhans, et al., "Sensitive Self-Driven Single-Component Organic Photodetector Based on Vapor-Deposited Small Molecules," *Advanced Materials* 36 (2024): 2402834.

19. Y. Li, R. A. Pacalaj, Y. Luo, et al., "Molecular Control of the Donor/Acceptor Interface Suppresses Charge Recombination Enabling High-Efficiency Single-Component Organic Solar Cells," *Advanced Materials* 37 (2025): 2409212.

20. J. Roncali, "Single-Material Organic Solar Cells Based on Small Molecule Homojunctions: An Outdated Concept or a New Challenge for the Chemistry and Physics of Organic Photovoltaics?," *Advanced Energy Materials* 11 (2021): 2102987.

21. S. Nizamuddin, S. Nousheen, M. Navadharsana, et al., "A Review on the Development of Covalently Connected Donor–Acceptor Molecular Materials for Single-Component Organic Solar Cells," *Journal of Materials Chemistry A* 13 (2025): 11114–11133.

22. Y. He, N. Li, and C. J. Brabec, "Single-Component Organic Solar Cells with Competitive Performance," *Organic Materials* 03 (2021): 228–244.

23. B. Liu, H. Sun, J.-W. Lee, et al., "Efficient and Stable Organic Solar Cells Enabled by Multicomponent Photoactive Layer Based on One-pot Polymerization," *Nature Communications* 14 (2023): 967.

24. T. Vangerven, P. Verstappen, N. Patil, et al., "Elucidating Batch-to-Batch Variation Caused by Homocoupled Side Products in Solution-Processable Organic Solar Cells," *Chemistry of Materials* 28 (2016): 9088–9098.

25. S. Y. Park, C. Labanti, R. A. Pacalaj, et al., "The State-of-the-Art Solution-Processed Single Component Organic Photodetectors Achieved by Strong Quenching of Intermolecular Emissive State and High Quadrupole Moment in Non-Fullerene Acceptors," *Advanced Materials* 35 (2023): 2306655.

26. A. L. Mannanov, D. O. Balakirev, E. D. Papkovskaya, et al., "Spectrally Selective Full-Color Single-Component Organic Photodetectors Based on Donor-Acceptor Conjugated Molecules," *Molecules* 28 (2023): 368.

27. Y. N. Luponosov, A. N. Solodukhin, A. L. Mannanov, et al., "Effect of Oligothiophene π-bridge Length in D-π-A Star-shaped Small Molecules on Properties and Photovoltaic Performance in Single-component and Bulk Heterojunction Organic Solar Cells and photodetectors," *Materials Today Energy* 22 (2021): 100863.

28. G. Antoniou, P. Yuan, L. Koutsokeras, et al., "Low-power Supralinear Photocurrent Generation via Excited state Fusion in Single-component Nanostructured Organic Photodetectors," *Journal of Materials Chemistry C* 10 (2022): 7575–7585.

29. A. Pal, M. Gedda, and D. K. Goswami, "PTCDI-Ph Molecular Layer Stack-Based Highly Crystalline Microneedles as Single-Component Efficient Photodetector," *ACS Applied Electronic Materials* 4 (2022): 946–954.

30. M. Wang, Y.-Z. Li, H.-C. Chen, et al., "Unveiling the Underlying Mechanism of Record-high Efficiency Organic near-infrared Photodetector Harnessing a Single-component Photoactive Layer," *Materials Horizons* 7 (2020): 1171–1179.

31. R. K. Canjeevaram Balasubramanyam, A. E. Kandjani, C. J. Harrison, et al., "1,4-Dihydropyrrolo[3,2- b]pyrroles as a Single Component Photoactive Layer: A New Paradigm for Broadband Detection," *ACS Applied Materials & Interfaces* 9 (2017): 27875–27882.

32. A. Rana, S. Y. Park, C. Labanti, et al., "Octupole Moment Driven Free Charge Generation in Partially Chlorinated Subphthalocyanine for Planar Heterojunction Organic Photodetectors," *Nature Communications* 15 (2024): 5058.

33. V. C. Nikolis, Y. Dong, J. Kublitski, et al., "Field Effect versus Driving Force: Charge Generation in Small-Molecule Organic Solar Cells," *Advanced Energy Materials* 10 (2020): 2002124.

34. H. T. Chandran, T.-W. Ng, Y. Foo, et al., "Direct Free Carrier Photogeneration in Single Layer and Stacked Organic Photovoltaic Devices," *Advanced Materials* 29 (2017): 1606909.

35. S. Olthof, R. Meerheim, M. Schober, and K. Leo, "Energy Level Alignment at the Interfaces in a Multilayer Organic Light-emitting Diode Structure," *Physical Review B* 79 (2009): 245308.

36. S. Scholz, C. Corten, K. Walzer, D. Kuckling, and K. Leo, "Photochemical Reactions in Organic Semiconductor Thin Films," *Organic Electronics* 8 (2007): 709–717.

37. J. Huang, M. Pfeiffer, A. Werner, J. Blochwitz, K. Leo, and S. Liu, "Low-Voltage Organic Electroluminescent Devices Using *Pin* Structures," *Applied Physics Letters* 80 (2002): 139–141.

38. Y. Chen, X. Liu, S. Braun, Y. Wang, and M. Fahlman, "Image-force Effects on Energy Level Alignment at Electron Transport Material/Cathode Interfaces," *Journal of Materials Chemistry* 8 (2020): 173.

39. Y. Dong, V. C. Nikolis, F. Talnack, et al., "Orientation Dependent Molecular Electrostatics Drives Efficient Charge Generation in Homojunction Organic Solar Cells," *Nature Communications* 11 (2020): 4617.

40. X. Yu, Q. Zhou, T. Zheng, et al., "Interface Engineering for Achieving Efficient and Stable Perovskite Solar Cells by Bphen-fullerene Dimer," *Chemical Engineering Journal* 452 (2023): 139412.

41. X. Yao, Y. Li, Y. Sun, et al., "High External Quantum Efficiency and Ultra-Narrowband Organic Photodiodes Using Single-Component Photoabsorber With Multiple-Resonance Effect," *Advanced Materials* 37 (2025): 2414465.

42. G. Simone, M. J. Dyson, S. C. J. Meskers, R. A. J. Janssen, and G. H. Gelinck, "Organic Photodetectors and Their Application in Large Area and Flexible Image Sensors: the Role of Dark Current," *Advanced Functional Materials* 30 (2020): 1904205.

43. S. Machlup, "Noise in Semiconductors: Spectrum of a Two-Parameter Random Signal," *Journal of Applied Physics* 25 (1954): 341–343.

44. M. Daboczi, J. Kim, J. Lee, et al., "Towards Efficient Integrated Perovskite/Organic Bulk Heterojunction Solar Cells: Interfacial Energetic Requirement to Reduce Charge Carrier Recombination Losses," *Advanced Functional Materials* 30 (2020): 2001482.

45. M. Daboczi, I. Hamilton, S. Xu, et al., "Origin of Open-Circuit Voltage Losses in Perovskite Solar Cells Investigated by Surface Photovoltage Measurement," *ACS Applied Materials & Interfaces* 11 (2019): 46808–46817.

46. J. Luke, L. Corrêa, J. Rodrigues, et al., "A Commercial Benchmark: Light-Soaking Free, Fully Scalable, Large-Area Organic Solar Cells for Low-Light Applications," *Advanced Energy Materials* 11 (2021): 2003405.

47. B. T. van Gorkom, T. P. A. van der Pol, K. Datta, M. M. Wienk, and R. A. J. Janssen, "Revealing Defective Interfaces in Perovskite Solar Cells From Highly Sensitive Sub-bandgap Photocurrent Spectroscopy Using Optical Cavities," *Nature Communications* 13 (2022): 349.

48. V. C. Nikolis, J. Benduhn, F. Holzmueller, et al., "Reducing Voltage Losses in Cascade Organic Solar Cells While Maintaining High External Quantum Efficiencies," *Advanced Energy Materials* 7 (2017): 1700855.

49. S. Gielen, C. Kaiser, F. Verstraeten, et al., "Intrinsic Detectivity Limits of Organic Near-Infrared Photodetectors," *Advanced Materials* 32 (2020): 2003818.

50. C. Labanti, Y. Sun, J. Luke, et al., "Breaking Crystallinity for Optimal Dark Current: Nonfullerene Acceptor Dilution as a Strategy for High-Performance Organic Photodetectors," *Advanced Optical Materials* 13 (2025): 2500255.

51. F. Verstraeten, S. Gielen, P. Verstappen, et al., "Near-infrared organic photodetectors based on bay-annulated indigo showing broadband absorption and high detectivities up to 1.1 μm," *Journal of Materials Chemistry C* 6 (2018): 11645–11650.

52. Z. Tang, Z. Ma, A. Sánchez-Díaz, et al., "Polymer:Fullerene Bimolecular Crystals for Near-Infrared Spectroscopic Photodetectors," *Advanced Materials* 29 (2017): 1702184.

53. C. Kaiser, K. S. Schellhammer, J. Benduhn, et al., "Manipulating the Charge Transfer Absorption for Narrowband Light Detection in the Near-Infrared," *Chemistry of Materials* 31 (2019): 9325–9330.

54. K. Vandewal, J. Benduhn, K. S. Schellhammer, et al., "Absorption Tails of Donor:C_{60} Blends Provide Insight Into Thermally Activated Charge-Transfer Processes and Polaron Relaxation," *Journal of the American Chemical Society* 139 (2017): 1699–1704.

55. X. Ma, H. Bin, B. T. Van Gorkom, et al., "Identification of the Origin of Ultralow Dark Currents in Organic Photodiodes," *Advanced Materials* 35 (2023): 2209598.

56. A.-L. Hofmann, J. Wolansky, M. Hambsch, et al., "Strategies to Control Crystal Growth of Highly Ordered Rubrene Thin Films for Application in Organic Photodetectors," *Advanced Optical Materials* 12 (2024): 2401025.

57. T. Zhang, L. C. Winkler, J. Wolansky, J. Schröder, K. Leo, and J. Benduhn, "High-Performance Filterless Blue Narrowband Organic Photodetectors," *Advanced Functional Materials* 34 (2024): 2308719.

58. T. Zhang, J. Schröder, J. Wolansky, K. Leo, and J. Benduhn, "Low-donor Content Approach to Achieve Sensitive Narrowband Organic Photodetectors," *Applied Physics Letters* 124 (2024): 193502.

59. J. Benduhn, K. Tvingstedt, F. Piersimoni, et al., "Intrinsic Non-radiative Voltage Losses in Fullerene-based Organic Solar Cells," *Nature Energy* 2 (2017): 17053.

60. G. M. Lee, T. H. Kim, Y. Kim, and J. W. Shim, "Noise Suppression in Organic Photodiodes: a Comprehensive Review of Mechanistic Insights and Design Principles," *Small* 22 (2026): 10935.

61. A. A. Balandin, "Low-frequency 1/*f* Noise in Graphene Devices," *Nature Nanotechnology* 8 (2013): 549–555.

62. Y. Wang, T. Zhang, D. Samigullina, et al., "Semitransparent Near-Infrared Organic Photodetectors: Flexible, Large-Area, and Physical-Vapor-Deposited for Versatile Advanced Optical Applications," *Advanced Functional Materials* 34 (2024): 2313689.

63. J. B. Lee, I.-N. Kang, J. W. Park, and S. Y. Oh, "Effects of Bphen Layer as Hole Blocking Material on the Performance of Vertical Type Light Emitting Transistor Using C_{60} and MEH-PPV," *Molecular Crystals and Liquid Crystals* 505 (2009): 1/[239]-8/[246].

64. N. Li, J. Lim, J. D. Azoulay, and T. Nga, "Tuning the Charge Blocking Layer to Enhance Photomultiplication in Organic Shortwave Infrared Photodetectors," *Journal of Materials Chemistry* 8 (2020): 15142.

65. R. Ceolin, M. Mariaud, P. Levillain, and N. Rodier, "Structure Cristalline de la Bathophénanthroline (Diphenyl-4,7 Phénanthroline-1,10)," *Acta Crystallographica* 35 (1979): 1630–1632.

66. J. Endres, I. Pelczer, B. P. Rand, and A. Kahn, "Determination of Energy Level Alignment within an Energy Cascade Organic Solar Cell," *Chemistry of Materials* 28 (2016): 794–801.

67. P.-H. Huang, Y.-H. Wang, J.-C. Ke, and C.-J. Huang, "Investigation of Various Active Layers for Their Performance on Organic Solar Cells," *Materials* 9 (2016): 667.

68. G. E. Morse, M. G. Helander, J. Stanwick, et al., "Experimentally Validated Model for the Prediction of the HOMO and LUMO Energy Levels of Boronsubphthalocyanines," *The Journal of Physical Chemistry C* 115 (2011): 11709–11718.

69. H. Wei, R. Zhang, G. Huang, C. Lv, and J. Tang, "Highly Stable and Efficient Tandem White Light Emitting Diodes Based on Efficient Electron Injection and Transport," *Journal of Materials Chemistry C* 10 (2022): 5994–6001.

70. Q. Wang, J. Yang, A. Gerlach, F. Schreiber, and S. Duhm, "Advanced characterization of organic–metal and organic–organic interfaces: From photoelectron spectroscopy data to energy-level diagrams," *Journal of Physics: Materials* 5 (2022): 044010.

71. J. Wu, J. Luke, H. K. H. Lee, et al., "Tail state Limited Photocurrent Collection of Thick Photoactive Layers in Organic Solar Cells," *Nature Communications* 10 (2019): 5159.

72. J. Wu, J. Lee, Y.-C. Chin, et al., "Exceptionally Low Charge Trapping Enables Highly Efficient Organic Bulk Heterojunction Solar Cells," *Energy & Environmental Science* 13 (2020): 2422–2430.

73. S. Naka, H. Okada, H. Onnagawa, and T. Tsutsui, "High Electron Mobility in Bathophenanthroline," *Applied Physics Letters* 76 (2000): 197–199.

74. Simojio Simulation Tool, accessed January, 2026, https://github.com/simoji-dev/simojio.

75. S. J. Byrnes, "Multilayer Optical Calculations," preprint, bioRxiv March 6, 2016, https://doi.org/10.48550/arXiv.1603.02720.

76. S. C. B. Mannsfeld, M. L. Tang, and Z. Bao, "Thin Film Structure of Triisopropylsilylethynyl-Functionalized Pentacene and Tetraceno[2,3-b]thiophene From Grazing Incidence X-Ray Diffraction," *Advanced Materials* 23 (2011): 127–131.

Supporting Information

Additional supporting information can be found online in the Supporting Information section.

Supporting File: adfm75690-sup-0001-SuppMat.docx.